Optics Letters

High-throughput screening of a high-Q mid-infrared Tamm emitter by material informatics

WANG XI, YIDA LIU, JINLIN SONG, RUN HU,* AND XIAOBING LUO

School of Energy and Power Engineering, Huazhong University of Science and Technology, Wuhan 430074, China
**Corresponding author: hurun@hust.edu.cn*

Received 14 December 2020; revised 14 January 2021; accepted 21 January 2021; posted 26 January 2021 (Doc. ID 417378); published 12 February 2021

Narrowband mid-infrared emitters, quantified by the *Q*-factor, have garnered a lot of attention due to their emerging applications from chemical and biosensing to efficient thermal utilization. Previous studies reported high *Q*-factor emitters within several selected wavelengths, still lacking a large database of emitter structures with very high *Q*-factors. In this Letter, we utilized the Monte Carlo Tree Search (MCTS) algorithm under the framework of material informatics to optimize the Tamm emitters at the infrared range (from 3 to 10 μm) for achieving a high *Q*-factor and high emissivity simultaneously, providing a large database of high and sharp emission peaks in the infrared. Through the MCTS algorithm, the structure with a *Q*-factor of 508 and an emissivity peak of 0.92 at 4.225 μm is obtained, far surpassing the previous results, and the underlying mechanism is discussed by electric field simulations. The high *Q*-factor emitters in the database show good monochromatism and high emissivity, accelerating the selection of proper perfect emitters for desired wavelengths. This Letter also paves a feasible avenue for the emitter and absorber design with ultrahigh monochromatism.

https://doi.org/10.1364/OL.417378

The mid-infrared (mid-IR) emitters are widely demanded for extensive applications in chemical and bio-sensing [1,2], thermophotovoltaics power generation [3], thermal management [4] thermal camouflage [5,6], etc. According to Planck's law, the thermal emission from most objects in nature is rather broadband, thus making the utilization efficiency of these electromagnetic (EM) waves in the IR range difficult and challenging. For example, the lighting efficiency of incandescent light bulbs is less than 10% due to the small fraction of visible light in the whole broad radiation spectrum, which is the exact reason why they are phased out globally now. Therefore, the narrowband mid-IR emitter with higher efficiency by tuning emission spectra is preferable for many applications. For instance, in the thermophotovoltaic (TPV) system, the input broadband thermal emission is tuned to be narrowband just above the energy bandgap of the p-n junction in the photovoltaic (PV) cells to improve the photocurrent and power generation efficiency, thus enabling the far breaking of the Shockley–Queisser limit [7]. Narrowband emission is also desired for infrared sensing and detecting, since the organic and gas molecules are sensitive to specific mid-IR emission, such as exhalation detection and toxic gas detection [8]. Moreover, narrowband thermal radiation can also spark ideas of new applications, such as selective radiative cooling [9,10] and fixed-wavelength photothermal sterilization [11].

To achieve narrowband mid-IR perfect emitters, people have proposed various methods and roadmaps. The original method was to combine broadband emission with a filter to produce narrowband radiation, which was both structurally bloated and inefficient. Thanks to nanophononics and metamaterials, a large variety of nanostructures have been investigated in the past few decades to exhibit a narrowband emission, such as quantum cascade lasers [12], metasurfaces [13,14], photonic crystal [15,16], multilayers [17,18], surface plasmons [19,20], and Tamm plasmons [21,22]. Among them, Tamm plasmon polaritons emerge with 1D structure and comprehensive performance.

Tamm plasmon polaritons was first found by Kaliteevski *et al*. [21] in the interface between the distributed Bragg reflector (DBR) and the metal layer, which is similar to the electronic state of Tamm surface of crystal interface. They analyzed the fundamental principle of the two types of Tamm radiators through the transfer matrix method (TMM). The characteristics of its narrowband emission and relatively simple structure attract much attention to narrow the emission peak at the resonant frequency, and the *Q*-factor is utilized to quantify the performance by dividing the Tamm plasmon polariton (TPP) resonance wavelength λ_{TPP} over the full width at half-maximum (FWHM). Yang *et al*. optimized the DBR period number and different metal substrates and obtained a Tamm emitter with five periods of Si/ SiO_2 DBR on an Au substrate with a *Q*-factor of 36.5 [23]. Wang *et al*. [22,24] and Zhu *et al*. [25] modified the regular Tamm structure and improved the *Q*-factor successively by thickening the first layer adjacent to the metal substrate or by inserting the optical cavity between the DBR and the metal layer. These studies only optimize the Tamm emitters by hand, and the mass of possible combinations of materials, structures, and configurations at broad wavelengths are not

explored yet. In this regard, the machine-learning optimization method, which has been applied successfully in other scenarios also with a huge massive of candidates, can be adapted to solve the problem [26,27]. Sakurai *et al*. [28] utilized the Bayesian algorithm to design a group of aperiodic multilayered Tamm emitters with Ge, Si, and SiO_2, and achieved strong narrowband emissions with emissivity of 0.99 at wavelengths of 5, 6, and 7 μm with Q-factors of 217, 273, and 233, respectively. Their work demonstrated the superiority of a machine-learning-based approach over the manual design, but still left room for further improvement on both the wavelength range and the Q-factor.

To provide a reference database for high-Q perfect emitters in a broadband wavelength, in this Letter, we adopted the Monte Carlo Tree Search (MCTS) algorithm in the framework of material informatics to screen the mid-IR perfect emitter [29]. Without loss of generality, we also took the one-dimensional (1D) Tamm emitters in the wavelength range of 3–10 μm as an example to demonstrate the feasibility of seeking high-Q selective perfect emitters. The underlying mechanism of narrowband emission is also discussed.

To begin with, the 1D Tamm emitter here is composed of nine-pair alternative layers of germanium (Ge) and silicon dioxide (SiO_2) on golden (Au) substrate. Ge and SiO_2 are commonly used material in a DBR with a negligible extinction coefficient, while Au is chosen for a good mirror with an excellent electrical field confinement effect for its negative dielectric constant in the infrared. The refractive indices of SiO_2, Ge, and Au can be referred to in E. Palik's book [30], Nunley's work [31] and Ordal's work [32], respectively. For such binary sequences in the SiO_2/Ge DBR, there will be $2^{18} = 262144$ kinds of possible structures. Moreover, we will repeat the optimization process for each wavelength step of 0.01 μm, so the total number of the possible candidates is as high as $2^{18} \times 700 = 183, 500, 800$. Obviously, such a large number of candidates disable most of the conventional optimization algorithms; thus, we turn to the MCTS algorithm under the framework of material informatics [29]. A typical MCTS optimization process constructs a search tree with each path from the root node to the leaf node representing a possible candidate. Each node is evaluated by a parameter named Upper Confidence Bound (UCB), which can be calculated as

$$\mathrm{UCB}_i = \frac{V_i}{n_i} + b\sqrt{\frac{2\ln n_{\mathrm{parent}}}{n_i}}, \tag{1}$$

where n_i and n_{parent} are the number of visits to the node i and its parent node, respectively, and V_i is dynamically updated by summing up all simulation merit of the candidates whose paths have passed by the node i. The value of UCB implies how promising it is to explore the child of the node. The optimization is essentially the iteration of four steps, including selection, expansion, simulation, and back propagation. At the beginning, a randomly chosen initial candidate will mark a path from the leaf node to the root node. Then the selection will explore the more promising child with a larger UCB value of each node. When there is a tie, such as reaching a node not explored before, since all of its child nodes have the same UCB value of infinity, expansion will randomly explore a child node until reaching the tree height, which will mark a new path from the root to the leaf. After that, simulation will be carried out to evaluate the performance of the new candidate. The former

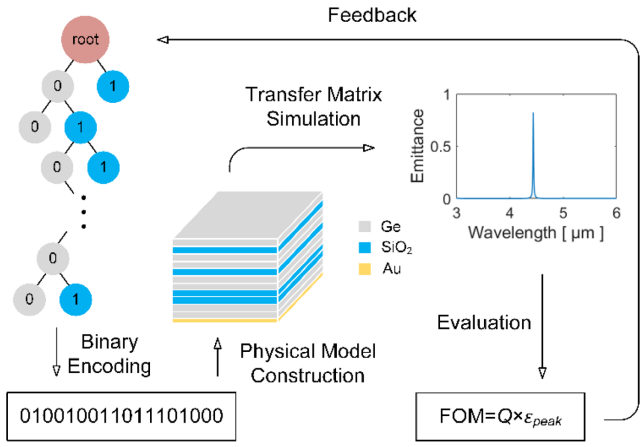

Fig. 1. Roadmap of the optimization.

three steps will change the search tree, and back propagation is finally needed to update the UCB of each node and prepare for the next round. To comply with MCTS, as shown in Fig. 1, we first encoded the Ge layer as a digit of 0 and SiO_2 layer as a digit of 1, respectively. Therefore, each Tamm structure corresponds to a digit sequence. The thickness of each sublayer is 0.21 μm, which was quantified by some preliminary parameter exploration. The Au substrate is 0.10 μm, which is thick enough to be opaque for the mid-IR EM wave. The emissivity spectrum of each digit sequence (Tamm emitter) is calculated by the TMM algorithm under the Kirchhoff's law. Then the peak emissivity $\varepsilon_{\mathrm{peak}}$ and Q-factor ($Q = \lambda_{\mathrm{TPP}}/\mathrm{FWHM}$) are identified from the emissivity spectrum. Note that only the Q-factor may not be meaningful, since the Q-factor only corresponds to the sharpness without requiring the absolute value of thermal emission energy. It is better to highlight the thermal emission energy and Q-factor simultaneously; thus, we define the figure of merit (FOM) parameter here as their product both to better implement our optimization and to maintain the physical meanings. The FOM defined here aims at finding all possible results with good wavelength-selectivity in the whole mid-IR, and we record all the calculated structures during the optimization. When applied to specific application with a fixed target wavelength λ_0, we can modify the FOM by multiplying a penalty factor f as $f = 1 - \varepsilon_{\mathrm{out}}/\varepsilon_{\mathrm{in}}$, where $\varepsilon_{\mathrm{out}}$ and $\varepsilon_{\mathrm{in}}$, respectively, represent the average emissivity out of and in the target band $\lambda_0 \pm \Delta\lambda$. The evaluation of a desired emissivity peak with $\varepsilon_{\mathrm{out}} \sim 0$ will not be weakened with $f \sim 1$, while the other candidates will be filtered. During the MCTS optimization, the Tamm emitters with the highest FOM value will be traced, and all the predicted structures and their emissivity spectra will be recorded for later analysis.

The tracings of the normalized Q-factor and FOM are shown in Fig. 2(a). It is seen that only 0.41% candidates are calculated to find a Tamm emitter with a high Q-factor up to 503, which is about 99.06% of the maximum Q-factor. Likewise, only 5.12% candidates are calculated to find a Tamm emitter with the maximum FOM. Such tracings vividly demonstrate the effectiveness of the MCTS optimization in finding the optimal structure. The corresponding emissivity spectra of the optimal structure with the maximum Q-factor are shown in Fig. 2(b). It is seen that the peak emissivity is 0.92 at 4.425 μm, and the Q-factor is as high as 508, which is quite a bit higher than most previous Q-factors for mid-IR emitters in the literature. Moreover, it

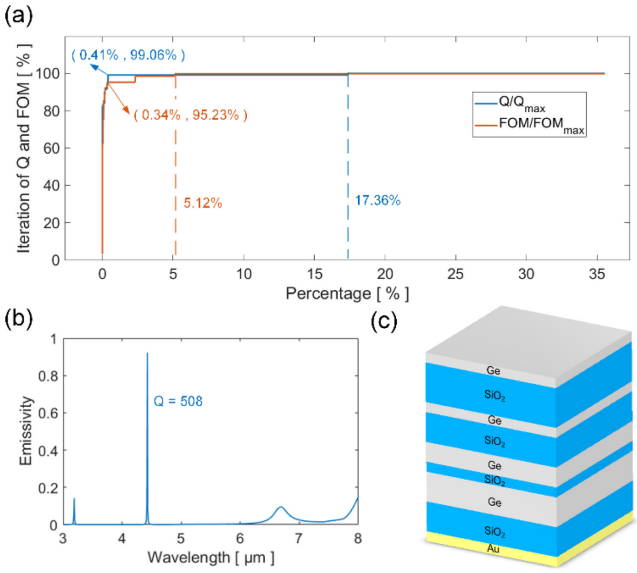

Fig. 2. (a) Tracing of the Q-factor and FOM versus iteration. (b) Corresponding spectrum of the globally optimal structure with a Q-factor of 508 and an emissivity peak of 0.92 at 4.225 μm. (c) Schematic of the optimal structure.

is seen that the emissivity at other wavelengths is rather small, implying that most thermal energy is emitted at the peak wavelength. This is a desired performance for a Tamm emitter with ultrahigh monochromatism in real applications. The corresponding Tamm emitter structure is illustrated in Fig. 2(c). Although there are 18 sublayers in the beginning, there are only eight layers in the end due to the material configurations, which is beneficial for the practical fabrication. Moreover, we find that the DBR structure is aperiodic, which is non-trial and cannot be designed by handwork.

As mentioned above, we record all the results with their Q-factor and peak emissivity ε_{peak} during the MCTS optimization process. From the calculated database, some typical emissivity spectra are selected within the range of 3 to 9 μm with an increase of 0.5 μm, as shown in Fig. 3(a), and the corresponding Q-factors are marked at the emissivity peaks. It is seen that for the wavelength from 3 to 9 μm, the Q-factor increases first to 484 at 4 μm and then drops to 11 at a peak wavelength of 9 μm. More specifically, the Q-factors with a peak wavelength below 5.5 μm will surpass 300, which are rather sharp and strong. It can also be noticed that structures with a high Q-factor also exhibit brilliant single-band characteristics. It originates from strong confinement of a photon which leads to suppression on unwanted resonance. More than the selected Tamm emitters, the structures with the highest Q-factor at each peak wavelength are plotted in Fig. 3(b) in the whole wavelength range and compared with the existing literature. The y axis denotes the Q-factor, while the color denotes the value of the peak emissivity. The scatter plot is consistent with the trend in Fig. 3(a) that the Q-factor increases first and drops at the wavelength larger than 4 μm. It can be seen that our optimized results defeat the existing work in most of the infrared with a higher Q-factor and brilliant peak emissivity ~1. To statistically analyze the scatter plot, we count the amount of Tamm emitters by the Q-factor and the peak wavelength ranges. As shown in Fig. 3(c), we ignore the less favorable results with a Q-factor below 100. The

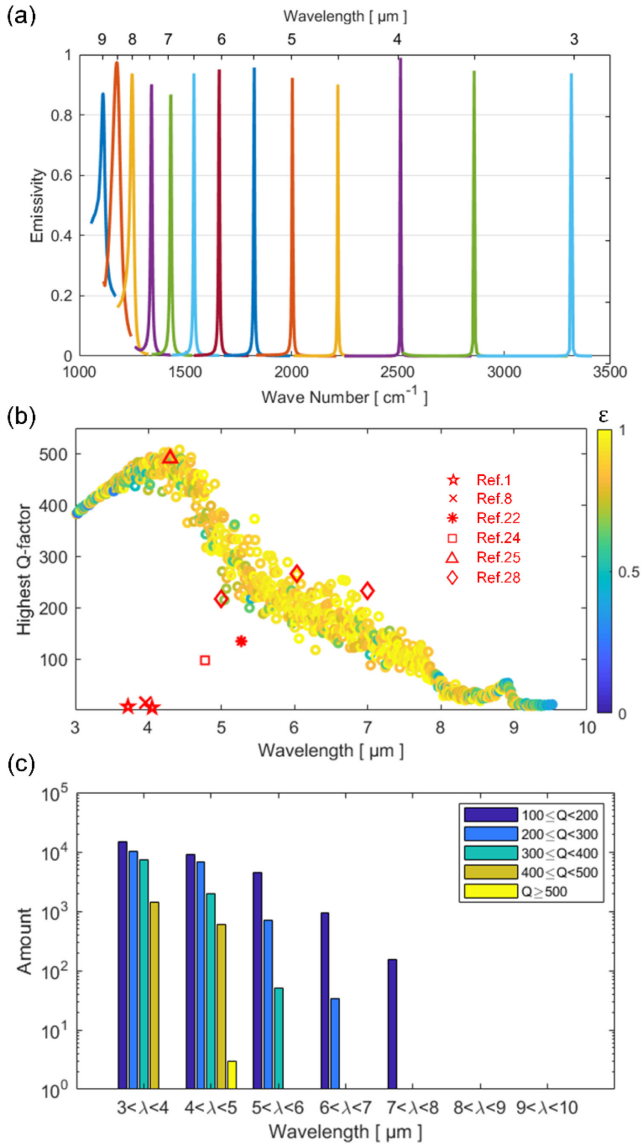

Fig. 3. (a) Several high Q-factors and strong emissivity results in each wavelength. (b) Highest Q-factor at each wavelength. Each point represents a similar emission peak in Fig. 2(b), with the color indicating the peak emissivity. (c) Distribution of a Q-factor above 100 in each wavelength range.

number of Tamm emitters in each Q-factor range decreases at higher peak wavelengths. It is seen that for the peak wavelength in 3–7 μm, the Tamm emitters tend to have a sharp emission with a Q-factor over 200, and over 300 only in 3–6 μm. In addition, these emission peaks with high Q-factors have strong wavelength selectivity with little unwanted peaks around, which is practically demanded with excellent monochromatism. The reason why there is little satisfying results in 8–11 μm is that the thickness of Ge and SiO_2 is a multiple of 0.21 μm, which tends to have a resonant wavelength at 3–4 μm. When the sublayers are thickened, more narrowband results are supposed to exhibit at longer wavelengths.

Figure 4 shows the normalized electric field intensity of three aperiodic multilayer structures. The first one is the optimal one with a Q-factor of 508, and the second and the third ones are randomly chosen with a resonant wavelength around 6 and

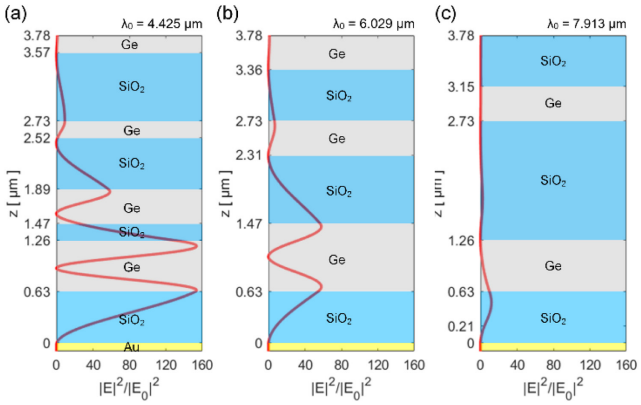

Fig. 4. Profile of normalized electric field intensity of some structures (a) $\lambda_0 = 4.425\ \mu m$, (b) $\lambda_0 = 6.029\ \mu m$, and (c) $\lambda_0 = 7.913\ \mu m$.

8 μm, respectively. For the optimal structure whose resonant wavelength lies in 4.425 μm, the electric field is strengthened at $z = 1.89\ \mu m$ and $z = 1.20\ \mu m$, and the amplitude of the electric field is six times and 10 times the incident amplitude, respectively. The electric fields of the second structure are also intensified at $z = 1.47\ \mu m$ and $z = 0.63\ \mu m$, although their resonant intensities are not as strong as the optimal one. Apart from them, the third one has a relatively poor enhancement on the electric field. These enhancements originate from the localized Tamm plasmon–polariton state formed between the dielectric mirror and metal. It has been proven that when two or more optimized defect layers are inserted between a quasi-periodic dielectric mirror and metal, the aperiodic structure can suppress some unnecessary emissivity peaks due to higher-order harmonics [28]. In our structures, the last three layers of the optimal structure and the last two layers of the second structure are regarded as effective cavities and induce strong confinement of photons which exhibit a Q-factor of 508 and 266, respectively. As a contrast, the third one lacks such quasicrystal-like composition, hence with a relatively low Q-factor of 72 and unsatisfactory performance. It can be inferred that Tamm emitters with high Q-factors and brilliant single-band character are more likely to have a structure with the optimized defect layer sandwiched between metal and quasi-periodic dielectric mirrors.

In summary, to build a reference database for narrowband mid-IR emitters, we designed a 1D Tamm emitter and optimized the structures in 3–10 μm to achieve a high Q-factor and high emissivity peak with the MCTS algorithm. More specifically, a Tamm emitter with a Q-factor of 508 at 4.225 μm was optimized, breaking the state-of-the-art Q-factor record of the SiO_2/Ge Tamm emitter. Our work provides not only a large database of high and sharp emission peaks in the wide mid-IR range for the Si/Ge emitter, but also a successful implementation example for other optimizations in terms of materials, dimensions, objective functions, etc.

Funding. National Natural Science Foundation of China (52076087); Wuhan City Science and Technology Program (2020010601012197).

Disclosures. The authors declare no conflicts of interest.

REFERENCES

1. A. T. Doan, T. Yokoyama, T. D. Dao, S. Ishii, A. Ohi, T. Nabatame, Y. Wada, S. Maruyama, and T. Nagao, Micromachines **10**, 413 (2019).
2. D. Rodrigo, O. Limaj, D. Janner, D. Etezadi, F. J. G. de Abajo, V. Pruneri, and H. Altug, Science **349**, 165 (2015).
3. Z. Zhou, O. Yehia, and P. Bermel, J. Nanophotonics **10**, 016014 (2016).
4. K. Amemiya, H. Koshikawa, M. Imbe, T. Yamaki, and H. Shitomi, J. Mater. Chem. C **7**, 5418 (2019).
5. H. Z. Zhu, Q. Li, C. Q. Zheng, Y. Hong, Z. Q. Xu, H. Wang, W. D. Shen, S. Kaur, P. Ghosh, and M. Qiu, Light Sci. Appl. **9**, 60 (2020).
6. Z. Q. Xu, Q. Li, K. K. Du, S. W. Long, Y. Yang, X. Cao, H. Luo, H. Z. Zhu, P. Ghosh, W. D. Shen, and M. Qiu, Laser Photonics Rev. **14**, 1900162 (2020).
7. L. P. Wang and Z. M. Zhang, Appl. Phys. Lett. **100**, 063902 (2012).
8. A. Lochbaum, Y. Fedoryshyn, A. Dorodnyy, U. Koch, C. Hafner, and J. Leuthold, ACS Photonics **4**, 1371 (2017).
9. J. J. Geffet, R. Carminati, K. Joulain, J. P. Mulet, S. P. Mainguy, and Y. Chen, Nature **416**, 61 (2002).
10. J. Guo, S. H. Ju, and J. Shiomi, Opt. Lett. **45**, 343 (2020).
11. L. Tan, J. Li, X. Liu, Z. Cui, X. Yang, S. Zhu, Z. Li, X. Yuan, Y. Zheng, K. W. K. Yeung, H. Pan, X. Wang, and S. Wu, Adv. Mater. **30**, 1801808 (2018).
12. Y. Yao, A. J. Hoffman, and C. F. Gmachl, Nat. Photonics **6**, 432 (2012).
13. Y. Liu, J. Song, W. Zhao, X. Ren, Q. Cheng, X. Luo, N. Fang, and R. Hu, Nanophotonics **9**, 855 (2020).
14. S. Jinlin, H. Shiyao, M. Yupu, C. Qiang, H. Run, and L. Xiaobing, Opt. Express **28**, 875 (2020).
15. N. P. de Leon, B. J. Shields, C. L. Yu, D. E. Englund, A. V. Akimov, M. D. Lukin, and H. Park, Phys. Rev. Lett. **108**, 226803 (2012).
16. M. U. Pralle, N. Moelders, M. P. McNeal, I. Puscasu, A. C. Greenwald, J. T. Daly, E. A. Johnson, T. George, D. S. Choi, I. El-Kady, and R. Biswas, Appl. Phys. Lett. **81**, 4685 (2002).
17. M. J. He, H. Qi, Y. F. Wang, Y. T. Ren, W. H. Cai, and L. M. Ruan, Opt. Express **27**, A953 (2019).
18. R. Hu, J. Song, Y. Liu, W. Xi, Y. Zhao, X. Yu, Q. Cheng, G. Tao, and X. Luo, Nano Energy **72**, 104687 (2020).
19. K. Ikeda, H. T. Miyazaki, T. Kasaya, K. Yamamoto, Y. Inoue, K. Fujimura, T. Kanakugi, M. Okada, K. Hatade, and S. Kitagawa, Appl. Phys. Lett. **92**, 021117 (2008).
20. F. Le, D. W. Brandl, Y. A. Urzhumov, H. Wang, J. Kundu, N. J. Halas, J. Aizpurua, and P. Nordlander, ACS Nano **2**, 707 (2008).
21. M. Kaliteevski, I. Iorsh, S. Brand, R. A. Abram, J. M. Chamberlain, A. V. Kavokin, and I. A. Shelykh, Phys. Rev. B **76**, 165415 (2007).
22. Z. Wang, J. K. Clark, Y.-L. Ho, B. Vilquin, H. Daiguji, and J.-J. Delaunay, ACS Photonics **5**, 2446 (2018).
23. Z. Y. Yang, S. Ishii, T. Yokoyama, T. D. Dao, M. G. Sun, P. S. Pankin, I. V. Timofeev, T. Nagao, and K. P. Chen, ACS Photonics **4**, 2212 (2017).
24. Z. Wang, J. K. Clark, Y.-L. Ho, B. Vilquin, H. Daiguji, and J.-J. Delaunay, Appl. Phys. Lett. **113**, 161104 (2018).
25. H. Z. Zhu, H. Luo, Q. Li, D. Zhao, L. Cai, K. K. Du, Z. Q. Xu, P. Ghosh, and M. Qiu, Opt. Lett. **43**, 5230 (2018).
26. R. Hu, S. Iwamoto, L. Feng, S. Ju, S. Hu, M. Ohnishi, N. Nagai, K. Hirakawa, and J. Shiomi, Phys. Rev. X **10**, 021050 (2020).
27. P. Chakraborty, Y. Liu, T. Ma, X. Guo, L. Cao, R. Hu, and Y. Wang, ACS Appl. Mater. Interfaces **12**, 8795 (2020).
28. A. Sakurai, K. Yada, T. Simomura, S. Ju, M. Kashiwagi, H. Okada, T. Nagao, K. Tsuda, and J. Shiomi, ACS Central Sci. **5**, 319 (2019).
29. T. M. Dieb, S. Ju, K. Yoshizoe, Z. Hou, J. Shiomi, and K. Tsuda, Sci. Technol. Adv. Mat. **18**, 498 (2017).
30. H. R. Philipp, in *Handbook of Optical Constants of Solids*, E. D. Palik, ed. (Academic, 1997), pp. 719–747.
31. T. N. Nunley, N. S. Fernando, N. Samarasingha, J. M. Moya, C. M. Nelson, A. A. Medina, and S. Zollner, J. Vac. Sci. Technol. B **34**, 061205 (2016).
32. M. A. Ordal, R. J. Bell, R. W. Alexander, Jr., L. L. Long, and M. R. Querry, Appl. Opt. **26**, 744 (1987).